Nano Research

Open Access

Research Article

Interlayer coupling enables EPC-linked polarity inversion and enhanced heat dissipation in MoS_2/CrOCl heterostructures

Jing Yang[1,2], Tao Zhu[1,3], Wanqian Wang[1,2], Chayuan Zeng[1,2], Jinghuan Xian[3], ShuFang Luo[1,2], Hongmei Zhang[1,2], Guang Wang[1,2], Wei Luo[1,2], Gang Peng[1,2], and Chuyun Deng[1,2] ✉

[1] College of Science, National University of Defense Technology, Changsha 410073, China
[2] Hunan Research Center of the Basic Discipline for Physical States, National University of Defense Technology, Changsha 410073, China
[3] College of Physical Science and Technology, Xiamen University, Xiamen 361005, China

Cite this article: *Nano Research*, **2026**, *19*, 94908743. https://doi.org/10.26599/NR.2026.94908743

ABSTRACT: Interlayer coupling is a central knob for engineering electronic reconstruction and energy dissipation in van der Waals heterostructures. However, a unified understanding that connects interlayer coupling to both electrical and thermal responses is still lacking. Electron–phonon coupling (EPC) could bridge this gap by linking interlayer coupling to both momentum and energy relaxation. Here we establish an electron–phonon-coupling-linked interpretation in MoS_2/CrOCl heterostructures, where interlayer coupling-driven interfacial charge transfer reshapes the MoS_2 electronic structure and, at the same time, renormalizes electron–phonon interactions that govern momentum relaxation and carrier–lattice energy relaxation. By using Raman and second-harmonic-generation (SHG) fingerprints, we identify 2L-MoS_2/CrOCl as the strongest coupling configuration. This is evidenced by the largest change in mode separation of 1.29 cm^{-1} and a pronounced SHG suppression from 100% to 11.9% relative to pristine MoS_2. In this regime, interfacial charge redistribution downshifts the MoS_2 Fermi level and converts its native n-type character to p-type conduction. Along with electrical transport experiments, we also study the thermal transport and characterize the steady-state temperature rise through scanning thermal microscopy. The MoS_2/CrOCl heterostructure exhibits more efficient heat evacuation, reducing the temperature rise by 38.5% under identical thermal loading conditions compared with the situation for pristine MoS_2 on SiO_2/Si. According to the observed EPC-linked electron and phonon transport properties, interlayer coupling in MoS_2/CrOCl heterostructure has induced both carrier-polarity inversion and enhanced interfacial heat dissipation, providing a basis for codesigning electro-thermal multifunctional devices.

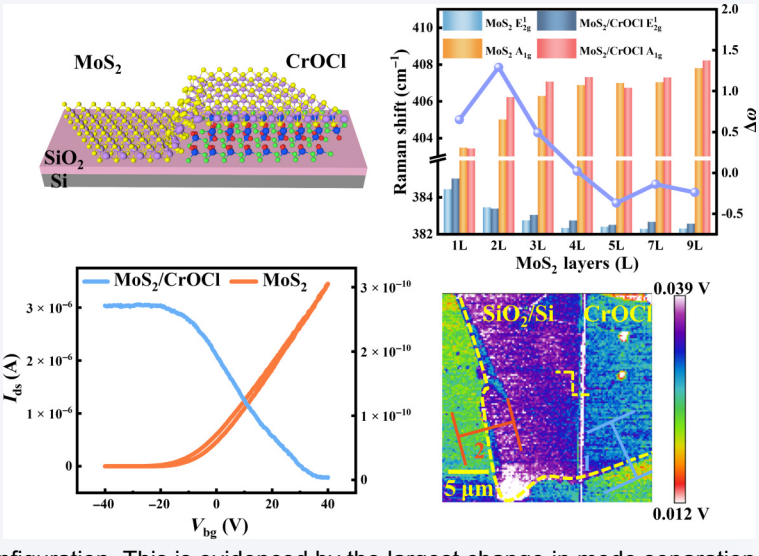

KEYWORDS: interlayer coupling, MoS_2/CrOCl, electron–phonon coupling, carrier-polarity inversion, heat dissipation

1 Introduction

Via moiré engineering, external fields, and hydrostatic pressure, a wide range of interfacial properties in van der Waals (vdW) heterostructures can be tuned, including charge transport, symmetry responses, and heat dissipation [1–6]. Among them, tuning electrical and thermal characteristics is crucial for enhancing device performance and reliability. These approaches work essentially by modulating the effective interlayer coupling, which strongly reshapes the interfacial electronic structure and lattice dynamics [7]. For example, interlayer coupling could lead to symmetry breaking, interfacial charge transfer, and phonon renormalization in MoS_2-based vdW heterostructures [1, 8, 9].

Received: February 5, 2026; **Revised:** March 25, 2026
Accepted: April 17, 2026

✉Address correspondence to dengchuyun@nudt.edu.cn

Interlayer coupling has also been shown to effectively modulate thermal transport as well as electronic structure. For instance, in graphene/MoS_2 heterostructures, the interfacial thermal conductance G increases with the interfacial coupling strength [10]. However, existing studies have rarely established a direct connection from the interlayer coupling to electron and phonon transport. How coupling-induced interfacial charge redistribution further jointly affects electrical transport and heat dissipation performance still lacks a unified understanding.

With twofold influences on both carrier transport dynamics and thermal transport dynamics, electron–phonon coupling (EPC) provides an ideal path towards deeper comprehension on interlayer coupling. EPC affects momentum relaxation that limits carrier mobility and electrical transport, while it mediates carrier-to-lattice energy relaxation that governs hot-carrier cooling and heat release [11, 12]. Importantly, interlayer coupling modifies interfacial hybridization and band alignment, thereby driving interfacial charge redistribution and a corresponding Fermi-level shift. Such charge redistribution not only changes the available electron–phonon scattering phase space, but can also alter the carrier screening environment of the phonon-induced perturbation potential, thereby renormalizing the screened electron–phonon matrix elements [13, 14]. As a result, EPC can be modulated through both scattering phase space and matrix-element renormalization, allowing interlayer coupling to simultaneously influence electrical and thermal transport [13–15]. Consistent with this picture, Raman measurements on twisted bilayer MoS_2 have revealed pronounced interlayer coupling-induced phonon renormalization associated with moiré-lattice reconstruction [16]. Moreover, sufficiently strong interlayer interaction may enable interlayer EPC channels, offering additional pathways for interfacial energy transfer [17].

Inspired by these EPC-related studies, we systematically investigated interlayer coupling in MoS_2/CrOCl heterostructures. According to our previous report, CrOCl could form strong vdW coupling with MoS_2, enabling pronounced interfacial charge transfer, while its high and anisotropic thermal conductivity provides an efficient heat-spreading pathway [18]. The coexistence of strong interfacial charge transfer and efficient heat spreading characteristics renders MoS_2/CrOCl an ideal platform for investigating how interlayer coupling simultaneously affects electrical transport and heat dissipation through EPC-linked interpretation. To this end, we fabricated thickness-dependent MoS_2/CrOCl heterostructures and evaluated the interlayer coupling effect via Raman and second-harmonic generation (SHG). The strongest coupling configuration is observed to be 2L-MoS_2/CrOCl, as evidenced by the largest change in mode separation of 1.29 cm^{-1} and a pronounced SHG suppression from 100% to 11.9% relative to pristine MoS_2. Driven by strong interlayer coupling, the depletion of electrons in MoS_2 and the consequent downshift of its Fermi level enable a gate-tunable polarity inversion. Such tunability unlocks potential polarity-programmable applications. Scanning thermal microscopy (SThM) further shows more efficient heat evacuation in MoS_2/CrOCl, with the temperature rise reduced by 38.5% compared with the situation for MoS_2 on SiO_2/Si. Overall, our results establish interlayer coupling as a practical knob for codesigning electrical polarity and thermal management in vdW heterostructures.

2 Results and discussion

In our experiments, MoS_2 flakes with well-defined thicknesses (1–9 layers, 1L–9L) were prepared by mechanical exfoliation from bulk MoS_2 crystals, using polydimethylsiloxane (PDMS) as the transfer medium. As shown in Fig. 1(d), layer numbers (1L–9L) were determined by combining atomic force microscopy (AFM) line profiles with previous literature calibration. On SiO_2/Si, monolayer MoS_2 typically shows an apparent AFM height of 0.8–1.0 nm, which can be larger than the pristine thickness of MoS_2 due to interfacial adsorbate effects. For thicker regions, the thickness increases stepwise by 0.6–0.7 nm per added layer, consistent with the crystallographic interlayer spacing of 3R-MoS_2 (~ 0.62 nm), establishing the thickness–layer correspondence used here [19]. To further validate the layer assignment, the characteristic Raman spectra of our samples show excellent agreement with standard layer-dependent Raman spectra (Fig. S5 in the Electronic Supplementary Material (ESM)) [20]. We investigated the interlayer coupling between MoS_2 and CrOCl by dry-transferring a MoS_2 flake onto a pre-exfoliated approximately 13-layer CrOCl flake on SiO_2/Si (Fig. S1 in the ESM). The CrOCl flake used in this work has a thickness of 12 nm, as confirmed by AFM (Fig. S2 in the ESM). This thickness lies within the thin-flake regime, where CrOCl has been reported to support strong interfacial coupling while preserving pronounced in-plane thermal anisotropy [9, 21].

To enhance the interfacial contact and coupling, the resulting heterostructure was subsequently annealed at 120 °C for 2 h under an argon atmosphere. Figures 1(a) and 1(b) show the schematic illustration and optical microscopy (OM) image of the MoS_2/CrOCl heterostructure, respectively. As shown in Fig. 1(b), the orange, red, yellow, blue, and purple dashed lines correspond to 1L, 2L, 3L, 5L, and 9L MoS_2 stacked on CrOCl, respectively. Notably, the entire region of the MoS_2/CrOCl heterostructure displayed a clear and uniform morphology under OM, with no cracks or wrinkles observed. These features directly indicate good interfacial contact quality between MoS_2 and CrOCl. This conclusion was further corroborated by AFM (Fig. 1(c)) and Raman mapping (Fig. S4 in the ESM).

SHG is a symmetry-sensitive optical probe in vdW heterostructures, because interlayer coupling can modify lattice symmetry and electronic structure, thereby strongly modulating the effective second-order nonlinear susceptibility $\chi^{(2)}$ [22–24]. Here we employed SHG as an experimentally accessible and symmetry-sensitive indicator of interlayer coupling in the MoS_2/CrOCl heterostructure. After calibrating the MoS_2 thickness by AFM, spatially resolved SHG spectra (Fig. 1(e)) acquired across disparate regions show a clear suppression of SHG intensity upon heterostructure formation for all tested layers. Quantitatively, the SHG intensities are reduced to 19.3%, 11.9%, 15.2%, 18.4%, and 15.8% of their respective pristine values for 1L, 2L, 3L, 5L, and 9L MoS_2, as shown by the purple solid line in Fig. 2(i). Notably, the suppression exhibits a pronounced nonmonotonic layer dependence and reaches its maximum for 2L-MoS_2/CrOCl, where the SHG intensity decreases to 11.9% of the pristine value. This nonmonotonic SHG modulation likely reflects a competition between the intrinsically thickness-enhanced SHG of 3R-MoS_2 and the interface-induced symmetry perturbation introduced by CrOCl. The especially strong suppression in 2L-MoS_2/CrOCl may result from the high sensitivity of bilayer 3R-MoS_2 to interfacial perturbations and the efficient transmission of such perturbations across the entire bilayer.

To elucidate the thickness-dependent SHG suppression in MoS_2/CrOCl heterostructures, we probed interlayer coupling from the lattice-vibration perspective. Figure 2(a) shows a representative Raman spectrum acquired from the MoS_2/CrOCl heterostructure

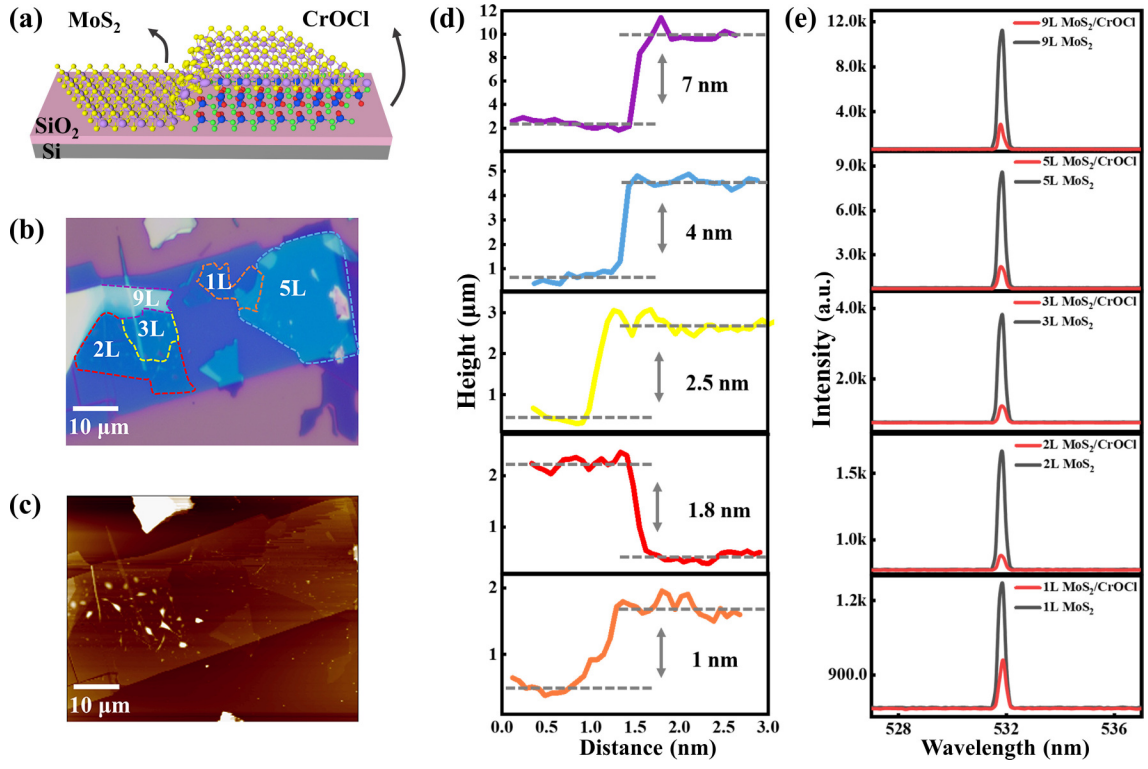

Figure 1 Fabrication and structural characterization of MoS_2/CrOCl heterostructures. (a) Schematic illustration of the MoS_2/CrOCl heterostructure fabrication process on SiO_2/Si substrates. (b) OM image of the MoS_2/CrOCl heterostructure, where the orange, red, yellow, blue, and purple dashed lines correspond to 1L, 2L, 3L, 5L, and 9L MoS_2 stacked on CrOCl, respectively. Scale bar: 10 μm. (c) AFM topographic image of the MoS_2/CrOCl heterostructure. (d) AFM line profile for different numbers of MoS_2 layers. Scale bar: 10 μm. (e) Room-temperature SHG spectra of pristine MoS_2 (black curve) with 1L–9L and the MoS_2/CrOCl heterostructure (red curve) formed therefrom.

region. The prominent peaks at ~ 383.5 and ~ 405.0 cm^{-1} are assigned to the in-plane E^1_{2g} and out-of-plane A_{1g} modes of MoS_2, while the peaks at ~ 207.4, ~ 415.1, and ~ 455.4 cm^{-1} attributed to the A^1_g, A^2_g, and A^3_g modes of CrOCl, respectively [1]. After annealing, both phonon modes of MoS_2 exhibited blueshifts, with A_{1g} and E^1_{2g} shifting by 1.39 and 0.27 cm^{-1}, respectively, increasing the mode separation $\Delta\omega$ from 21.70 to 22.82 cm^{-1} (Fig. 2(b)). Since thermal annealing is known to effectively remove interfacial residues and enhance intimate interlayer contact at vdW interfaces, the increased $\Delta\omega$ provides evidence that interlayer coupling is strengthened (Fig. S3 in the ESM) [25, 26]. Motivated by this observation, we further performed Raman measurements on pristine MoS_2 flakes (1L–9L) and the corresponding MoS_2/CrOCl heterostructures (Fig. S5 in the ESM). As summarized in Fig. 2(c), the A_{1g} mode exhibited a consistent blue shift (0.07–1.31 cm^{-1}) across all MoS_2 thicknesses (1L–9L), while the E^1_{2g} mode showed relatively small and thickness-dependent shifts. Notably, the change in mode separation systematically increases upon heterostructure formation and displays a distinct layer-number dependence, with the largest enhancement magnitude of 1.29 cm^{-1} observed for the 2L-MoS_2/CrOCl. This trend correlates with the SHG response (Fig. 2(i)): The 2L-MoS_2/CrOCl heterostructure also exhibited the strongest SHG suppression, with the SHG intensity reduced to 11.9% of its respective pristine value. Collectively, the consistent layer-dependent Raman and SHG fingerprints indicate that the 2L-MoS_2/CrOCl exhibits the strongest interlayer coupling regime among all the studied configurations. This thickness dependence suggests that interfacial charge transfer is the primary factor governing the coupling strength. Nevertheless, interfacial strain and other structural effects at the heterointerface may also modulate the final coupling response, particularly for non-2L heterostructures.

Given the intrinsically low symmetry of CrOCl, we performed polarization-resolved Raman spectroscopy on the 2L-MoS_2/CrOCl heterostructure to further probe interlayer coupling-induced symmetry reduction [27]. The sample was mounted on a rotational stage, with the horizontal direction defined as $\theta = 0°$. For pristine MoS_2 on SiO_2/Si, the E^1_{2g} and A_{1g} intensities remain unchanged with incident polarization under our scattering configuration, consistent with the high in-plane symmetry of MoS_2. In contrast, both modes in the 2L-MoS_2/CrOCl heterostructure exhibited a clear twofold symmetry in their angle-dependent Raman intensities, as shown in Figs. 2(e) and 2(f). As θ increased from 0° to 90°, the intensities of both modes progressively increased, yielding anisotropy ratios of ~ 1.45 for E^1_{2g} and ~ 2.05 for A_{1g} at 90° (intensity ratio defined as $I_{hetero}/I_{pristine}$). The contour map in Fig. 2(d) further visualized this symmetry-breaking behavior, with the A_{1g} mode showing more pronounced intensity modulation. The coupling-induced symmetry reduction is further supported by polarization-dependent SHG measurements. The SHG intensity can be described as $I(\theta) = I_0\cos^2(3\theta)$, where I_0 is the maximum SHG intensity, and θ is the angle between the incident polarization and the armchair (AC) axis of pristine MoS_2. As shown by the orange polar plot in Fig. 2(h), pristine MoS_2 exhibited a clear six-fold symmetry, which is typical characteristic of the D_{3h} point group. In contrast, the SHG response of the MoS_2/CrOCl heterostructure reveals a distinctly anisotropic intensity pattern (blue data in Fig. 2(h)), with SHG intensity enhanced along specific AC directions and suppressed along others, as further visualized in the

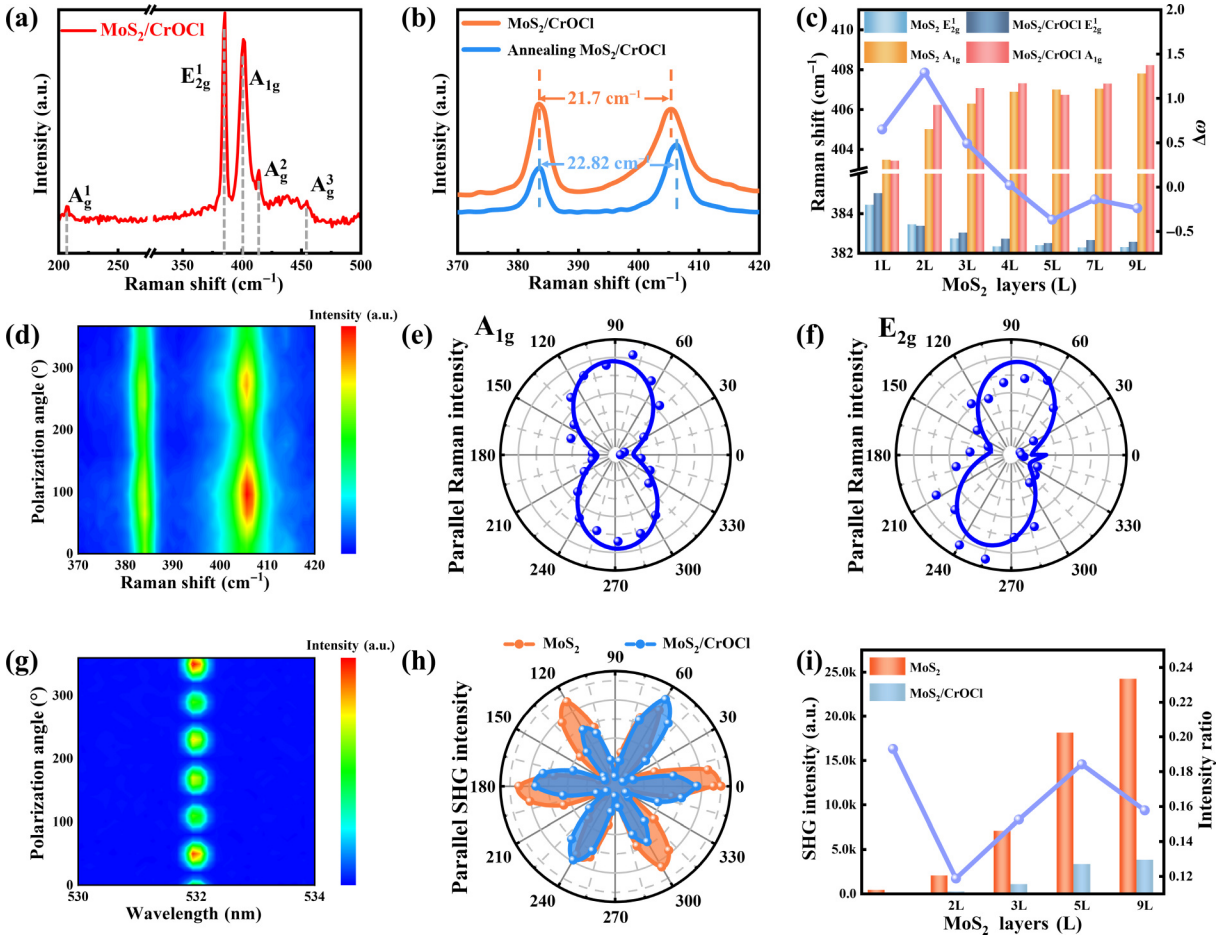

Figure 2 Probing thickness-dependent interlayer coupling in MoS_2/CrOCl heterostructures. (a) Raman spectrum of MoS_2/CrOCl heterostructures. (b) Raman spectra of the heterostructure before (orange) and after (blue) annealing. The dashed lines indicate the positions of E^1_{2g} and A_{1g} modes, with the mode separation defined as $\Delta\omega = \omega(A_{1g}) - \omega(E^1_{2g})$ (cm^{-1}). (c) Raman peak positions of E^1_{2g} and A_{1g} for pristine MoS_2 (1L–9L) and the constructed MoS_2/CrOCl heterostructures. The purple solid line indicates the change in mode separation of MoS_2 before and after stacking. ((d) and (g)) Contour maps of angle-dependent Raman and SHG intensity in the 2L-MoS_2/CrOCl heterostructure. ((e) and (f)) Polarization plots and fitted curves for E^1_{2g} and A_{1g} intensities, with blue dots denoting the experimental data. (h) Angle-resolved SHG intensity polarization map of the 2L-MoS_2/CrOCl heterostructure. (i) Summary bar plot of SHG intensity for 1L–9L pristine MoS_2 and the corresponding MoS_2/CrOCl heterostructure; the purple solid line represents the thickness-dependent SHG intensity ratio.

intensity contour map (Fig. 2(g)). Consistent symmetry breaking observed in both polarization-resolved Raman and SHG measurements provides robust evidence for pronounced interlayer coupling in the 2L-MoS_2/CrOCl heterostructure.

To elucidate the physical origin of the optical anisotropy induced by strong interlayer coupling, we further investigated interfacial interactions in the 2L-MoS_2/CrOCl heterostructure from the perspective of interfacial charge transfer. The peak positions of the A_{1g} and E^1_{2g} modes are sensitive to electron doping and strain, respectively, enabling us to quantitatively disentangle their contributions to the observed optical anisotropy [28–30]. As shown in Fig. 3(a), we compared the Raman spectra acquired from pristine MoS_2 on SiO_2/Si (q_1) and MoS_2/CrOCl heterostructure (q_2). At the point q_2, the A_{1g} mode exhibited a significant blue shift of 1.22 cm^{-1} with a reduced full width at half maximum (FWHM), while the E^1_{2g} mode showed a negligible red shift. This indicates a synergistic effect of interfacial charge transfer and strain at the heterointerface, where charge transfer dominates. This conclusion is consistent with the angle-dependent Raman contour map in Fig. 2(d), which showed higher anisotropy in the A_{1g} mode than in the E^1_{2g} mode.

To further corroborate the dominant role of interfacial charge transfer inferred from Raman analysis, we performed photoluminescence (PL) measurements, as the PL intensity and peak energy are highly sensitive to the exciton population and the renormalized optical transition energy [2, 31, 32]. As shown in Fig. S6 in the ESM, the heterostructure region (q_2) exhibited pronounced PL quenching accompanied by a clear blue shift of the A exciton peak ($\Delta E = 12$ meV), consistent with interfacial charge transfer behavior and suppressed radiative recombination due to efficient interfacial charge separation. We conducted Gaussian fitting on the A exciton emission (Figs. 3(b) and 3(c)) to elucidate the charge transfer mechanism and quantify corresponding transfer efficiency at the MoS_2/CrOCl heterointerface. The A exciton line shape can be divided into two components: the neutral exciton (A^0) originating from the pristine Coulomb interaction and the trion (A^-) dominated by carrier-doping effects [33]. For pristine 2L MoS_2 on SiO_2/Si (q_1, Fig. 3(b)), the emission was dominated by the A^- peak located at ~ 1.85 eV, indicative of n-type doping characteristics [34]. In contrast, in the MoS_2/CrOCl heterostructure region (q_2, Fig. 3(c)), the emission was dominated by the A^0 peak at ~ 1.89 eV, with its fitted area percentage increasing to nearly four times that of the pristine MoS_2 (Table S1 in the ESM). This marked

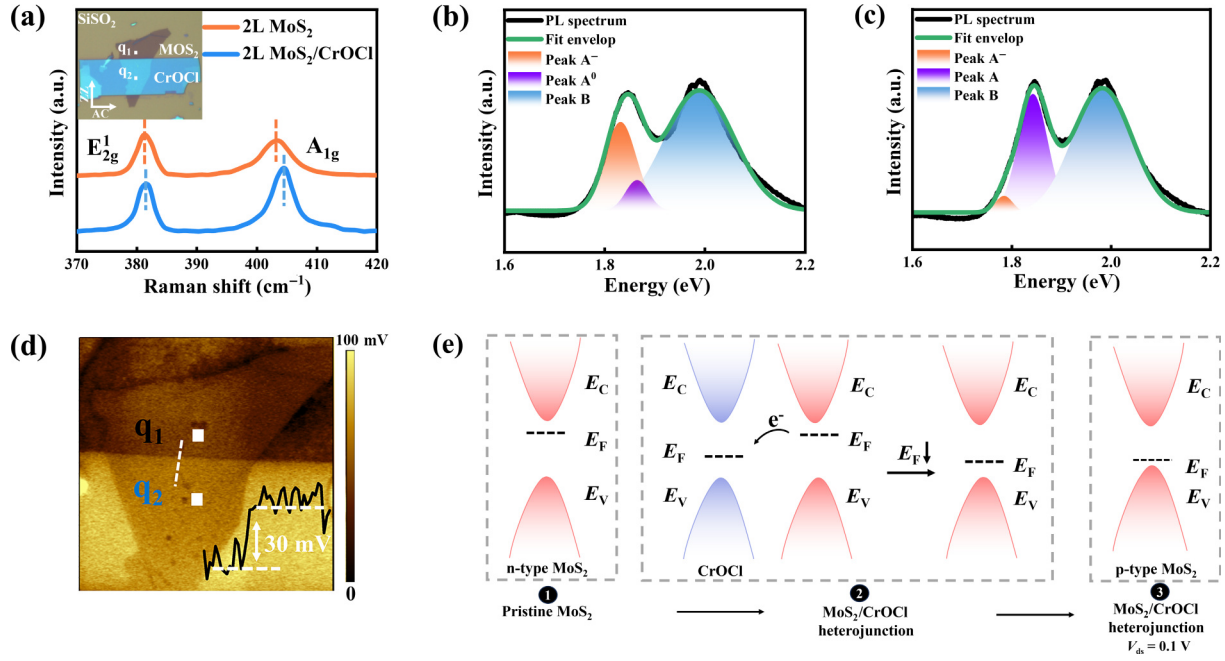

Figure 3 Charge Ttransfer in the 2L-MoS_2/CrOCl hHeterostructures driven by strong interlayer coupling. (a) Raman spectrum of the 2L-MoS_2/CrOCl heterostructure. Inset shows the OM image. Orange line: pristine MoS_2 on SiO_2/Si (point q_1). Blue line: MoS_2 on CrOCl (point q_2). ((b) and (c)) PL spectra extracted from points q_1 and q_2 in (a), showing the experimental PL intensity (black line) and fitted curve (green line), where the A exciton peak is decomposed into A^- and A^0 via a Gaussian function. (d) KPFM surface potential image of the 2L-MoS_2/CrOCl heterostructure, with the surface potential difference across the white dashed line shown in the bottom-right corner. (e) Density functional theory calculations of the band structures of 2L MoS_2 and CrOCl. Left panel: Band structure of pristine n-type 2L MoS_2. Middle panel: charge transfer at the interface during the heterostructure formation, inducing band realignment (Fermi level shifts toward the valence band of MoS_2). Right panel: applying a finite negative electric field ($V_{ds} = 0.1$ V, corresponding to a negative source-drain configuration) further lowers the Fermi level, resulting in p-type conduction characteristics for the heterostructure.

transition from trion-dominant to neutral-exciton-dominant PL provides spectroscopic evidence for a strong interlayer coupling-induced interfacial charge transfer from MoS_2 to CrOCl. To further validate this charge transfer process, we conducted Kelvin probe force microscopy (KPFM) measurements. As shown in Fig. 3(d), the surface potential in the heterostructure region (q_2) was ~ 30 mV higher than that in the pristine region (q_1), providing independent electrical evidence for the effective electron depletion in MoS_2 upon interfacing with CrOCl [2, 34]. These PL and KPFM signatures align with our previous studies on MoS_2/CrOCl heterostructures [1, 28], which revealed a higher KPFM surface potential in the MoS_2/CrOCl overlapping region than in pristine MoS_2. We deconvoluted the A exciton emission into neutral-exciton and trion components, then applied a trion mass-action model to quantify the extent of interfacial electron depletion in MoS_2. Here, the fitted area ratio A_{A^-}/A_{A^0} is used as a relative indicator of the free-electron population in MoS_2.

Based on the above optical and electrical evidence, we propose a schematic model illustrated in Fig. 3(e). In the absence of an external bias, 2L MoS_2 and CrOCl form a Type-II band-alignment heterostructure that favors interfacial charge separation, which commonly manifests as PL quenching in atomically thin heterostructures [31, 35]. Strong interlayer coupling can further renormalize the MoS_2 electronic structure and facilitate interfacial charge transfer from MoS_2 to CrOCl, consistent with the observed reduction of trion emission and the KPFM surface potential contrast [1]. The enhanced electron–hole separation in MoS_2 promotes the formation of indirect excitons, which predominantly recombine nonradiatively [36, 37]. Importantly, interfacial charge transfer causes a significant downward shift of the Fermi level in 2L MoS_2. Under a negative gate bias, the Fermi level is shifted further toward the valence-band maximum, endowing the system with pronounced p-type conduction. Thus, strong interlayer coupling-induced charge transfer provides an effective route to convert MoS_2 from its native n-type behavior toward p-type conduction [9, 38]. Beyond carrier-polarity control, interfacial charge redistribution induced by interlayer coupling offers a route to tune EPC, which concurrently governs electrical and thermal transport in vdW heterostructures [39]. Moreover, strong interlayer coupling may activate interlayer EPC channels, as has been directly observed in vdW stacks such as WSe_2/hexagonal boron nitride (hBN), where phonons in hBN are rendered Raman-active through interlayer resonant coupling to electronic transitions in the WSe_2, These interlayer channels provide additional cross-layer pathways for interfacial energy transfer [40].

As discussed above, the strongly coupled Type-II MoS_2/CrOCl vdW heterostructure drives charge transfer from MoS_2 to CrOCl. This process depletes electrons in MoS_2, downshifts its Fermi level, and enables gate-tunable polarity inversion. Moreover, the accompanying interfacial charge redistribution further modifies dielectric screening and can renormalize EPC, thus providing an additional handle to regulate heat dissipation. To verify the discussion, we fabricated MoS_2/CrOCl heterostructure field-effect transistors (FETs) and examined their gate-tunable electrical characteristics. In Fig. 4(a), the channel between electrodes 1 and 2 corresponds to pristine 2L MoS_2 FET, whereas the channel between electrodes 3 and 4 belongs to 2L-MoS_2/CrOCl heterostructure FET, with each constituent layer outlined by the green and red dashed lines, respectively. All the electrodes (5 nm Cr/70 nm Au) were fabricated via standard e-beam lithography and e-beam evaporation

to ensure reliable interfacial contacts. As shown in Fig. 4(b), both FETs exhibited near-Ohmic output characteristics in the low-bias regime, indicating that contact nonlinearity is not the dominant factor in the polarity characterization. More critically, the transfer characteristics provided direct evidence of carrier-polarity inversion in MoS_2. As shown in Fig. 4(c), the pristine 2L MoS_2 FET turned on under positive gate bias and exhibited a current on/off modulation exceeding four orders of magnitude (from ~ 10^{-10} to more than 2×10^{-6} A), consistent with the commonly observed n-type behavior of pristine MoS_2 arising from defect-related doping and Fermi-level pinning at metal–MoS_2 interfaces [41]. In contrast, the 2L-MoS_2/CrOCl FET exhibited unambiguous p-type conduction at $V_{ds} = 0.1$ V (Fig. 4(d)). Together with the optical evidence in Fig. 2, this result supports an electron-depletion mechanism: Strong interlayer coupling drives substantial interfacial charger transfer from MoS_2 to CrOCl, downshifting the Fermi level and stabilizing p-type transport under gate bias. This successful polarity inversion establishes a versatile platform for complementary electronics, enabling both n- and p-type operation from the same material through tailored interlayer coupling.

Beyond polarity inversion, such interlayer coupling-driven interfacial charge redistribution at the 2L-MoS_2/CrOCl interface is expected to reshape energy dissipation pathways through EPC. Guided by our EPC-linked interpretation, we quantitatively characterized the heat evacuation of the MoS_2/CrOCl heterostructure using SThM. A laser-heated resistive probe (configured in a Wheatstone bridge) exchanges heat with the sample upon contact, leading to a change in probe temperature that is transduced into an output voltage signal U. Following the established SThM framework, the relationship between the U and the thermal conductivity (κ) of the sample can be expressed as [42]

$$\frac{dU}{d(\kappa^{-1})} = \begin{cases} \frac{\beta Q}{\pi r}, \kappa < C \\ \frac{\beta Q}{2\pi\delta}\left(\ln\frac{\alpha}{vr} - \frac{3}{2}\right), \kappa \geq C \end{cases} \quad (1)$$

where β is a constant determined by the parameters of the Wheatstone bridge, Q is the heat flow from the thermal probe to the sample, r is the thermal contact radius, δ is the length of the cylindrical heat source, α is the thermal diffusivity, v is the scanning rate, and C is a probe-dependent conductivity scale factor. Through tight control of the scanning conditions and probe–sample contact, $\frac{\alpha}{vr}$ remains approximately constant during measurement, yielding a nearly linear dependence of the SThM output on κ^{-1} under our experimental operating regime. Consequently, after calibrating the probe voltage sensitivity coefficient (S), we convert the thermal signal to the corresponding

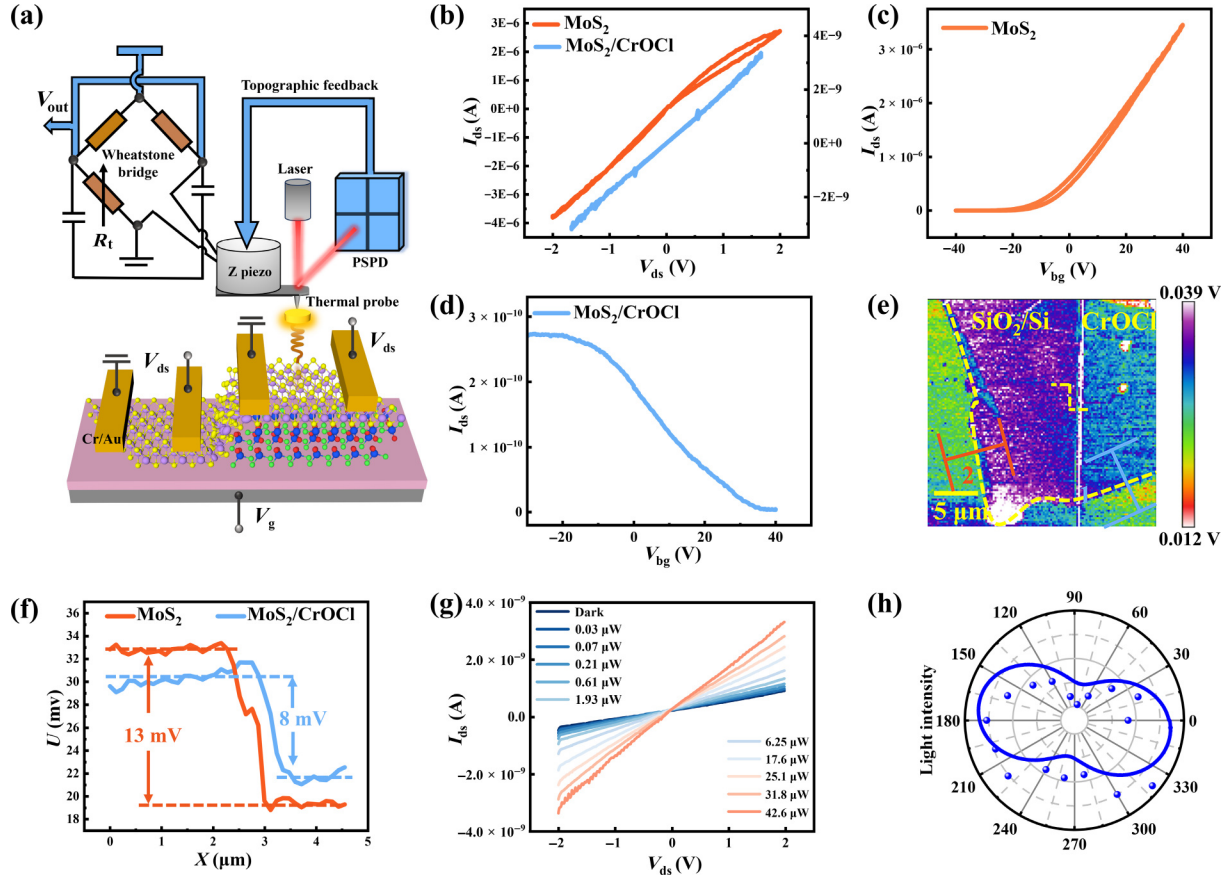

Figure 4 Polarity engineering and electro-thermal modulation in 2L MoS_2 via strong interlayer coupling with CrOCl. (a) Schematic diagram of the 2L-MoS_2/CrOCl heterostructure FET and the SThM configuration. The local temperature is probed using a thermoresistive sensor, whose output signal is read by a Wheatstone bridge circuit. (b) Output characteristics curves (I_{ds}–V_{ds}) of the pristine 2L MoS_2 FET (orange) and 2L-MoS_2/CrOCl heterostructure FET (blue) under low-bias regime, showing near-Ohmic behavior. ((c) and (d)) Transfer curves (I_{ds}–V_{bg}) of pristine 2L MoS_2 FET and 2L-MoS_2/CrOCl heterostructure FET, respectively, showing a clear polarity inversion from n-type to p-type conduction. (e) SThM image of the pristine MoS_2 region (left) and the MoS_2/CrOCl heterostructure region (right). Scale bar: 5 μm. (f) Corresponding thermal voltage line-scan profile extracted from (e). (g) Power-dependent photocurrent–voltage (I–V) characteristics of the 2L-MoS_2/CrOCl heterostructure under 532 nm illumination. (h) Angle-dependent photoresponse of the 2L-MoS_2/CrOCl heterostructure (polar plot).

temperature (T) rise via $T = \frac{U}{g \cdot S}$, where g is the lock-in amplifier gain factor [43]. The temperature in the 2L-MoS_2/CrOCl heterostructure was reduced by 38.5% compared with the situation for pristine MoS_2 on SiO_2/Si, confirming a significantly more efficient heat dissipation capability. Furthermore, based on the calibrated SThM contrast across the heterostructure (Figs. 4(e) and 4(f), and Fig. S8 in the ESM), the MoS_2/CrOCl region exhibits a thermal conductivity of ~ 1.63× higher than that of the pristine MoS_2 region.

These results indicate an interlayer coupling-enhanced heat dissipation pathway in the 2L-MoS_2/CrOCl heterostructure. Interlayer coupling drives interfacial charge transfer and establishes carrier screening, which could strongly renormalize EPC and accelerate electron to phonon energy relaxation [39]. Simultaneously, strong interlayer coupling introduces additional phonon-assisted interlayer energy transfer pathways, thereby enhancing heat flow from MoS_2 into CrOCl. Owing to the intrinsically high and anisotropic thermal conductivity of CrOCl, the injected heat spreads rapidly along the CrOCl layers, leading to a reduction of 38.5% in the local operating temperature of the heterostructure compared to the pristine MoS_2 [21]. Therefore, we established an EPC-linked approach to jointly tune electronic polarity and heat dissipation through the interlayer coupling, which help address challenges associated with both reconfigurable device functionality and thermal reliability in 2D electronics.

Combined with the reduced local temperature rise revealed by our SThM results, this thermal-management capability might help suppress local photothermal accumulation under laser illumination and thereby support more stable photocurrent output in the MoS_2/CrOCl photodetector [44]. Systematic characterizations revealed that the optoelectronic response of the MoS_2/CrOCl heterostructure could be effectively modulated by both the optical power and polarization state of the incident light. Under 532 nm illumination with incident power ranging from 0 to 42.6 μW, the output photocurrent increases monotonically with optical power (Fig. 4(g)), reaching a maximum responsivity of ~ 3.31 mA/W. This enhancement is primarily attributed to the improved separation and transport efficiency of the photogenerated carriers promoted by the strong interlayer coupling. Angle-resolved measurements reveal a robust two-fold symmetric photoresponse polarization polar pattern (Fig. 4(h)) with an anisotropy ratio of 1.08, which is attributable to symmetry breaking at the heterointerface. The obtained responsivity and anisotropy ratio are relatively modest compared with some recent related photodetectors [45]. Such performance is still physically reasonable for the present 2L-MoS_2/CrOCl heterostructure, where the polarization-dependent photoresponse mainly arises from interfacial symmetry breaking. The relatively low responsivity further indicates that the device is not yet optimized for maximum photogain. These results therefore support a proof-of-concept demonstration of interface-induced anisotropic photodetection.

3 Conclusions

We systematically investigated thickness-dependent interlayer coupling in MoS_2/CrOCl heterostructures and proposed an EPC-linked interpretation to elucidate how tunable interlayer coupling governs their structure–property relationships. We identify 2L-MoS_2/CrOCl as the strongest coupling configuration, evidenced by its largest change in mode separation of 1.29 cm^{-1}, and strong SHG suppression from 100% to 11.9% relative to pristine MoS_2. Through the strong interlayer coupling, interfacial charge redistribution downshifts the Fermi level of 2L MoS_2, converting its native n-type character into a p-type conduction, consistent with electrical transport measurements. Beyond polarity inversion, these SThM results further reveal enhanced heat dissipation, with the MoS_2/CrOCl heterostructure temperature rise suppressed by 38.5% compared with the pristine MoS_2 on SiO_2/Si. We attribute this electrical-thermal regulation to an interlayer coupling-enhanced EPC pathway, which reshapes carrier scattering and energy relaxation at the vdW interface. Photoresponse measurements additionally show a power-dependent nonlinear response with a pronounced twofold in-plane symmetry, consistent with anisotropic interfacial coupling. Overall, this work links interlayer coupling to electrical-thermal responses through EPC, providing practical guidelines for codesigning electro-thermal characteristics in vdW heterostructure devices.

4 Experimental section

4.1 Fabrication of MoS_2/CrOCl heterostructures

CrOCl flakes were mechanically exfoliated from bulk CrOCl crystals (Shanghai On-way Technology Co., Ltd.) using blue tape (Sunnano (Taizhou) New Energy Co., Ltd.) and transferred onto the surface of a 285 nm SiO_2/Si substrate doped with phosphorus. MoS_2 flakes (Shanghai On-way Technology Co., Ltd.) of various thicknesses were prepared using the same method. A piece of PDMS was attached to a glass slide. After placing a polyvinyl butyral (PVB) film on the PDMS surface, the glass slide was mounted on a micro-translation stage under an optical microscope with a 3D positioning adjustment platform. The PVB film was then gently brought into contact with the MoS_2 surface. After the PVB film covered the flake, the sample was heated to 60 °C for 2 min. The glass slide was subsequently lifted rapidly, leaving the MoS_2 on the PVB film. The PVB film carrying the MoS_2 was then transferred onto the exfoliated CrOCl flake, completing the heterostructure assembly via thermal release of the PVB film. Electrodes (5/70 nm Cr/Au) for the MoS_2/CrOCl heterostructure devices were fabricated using standard electron-beam lithography (Raith Eline Plus, Germany) and electron-beam evaporation procedures (TECHNOL TEMD500, China). For the representative device, channel length (L) was 7 μm, channel width (W) was 2 μm, and contact area (A_c) was 14 μm^2.

4.2 Morphological and spectroscopic characterization

The sample morphology was examined using OM (SOPTOP). The thickness and surface potential were characterized using AFM and KPFM (NT-MDT NTEGRA P9, Russia). Raman and PL spectra were acquired using a confocal Raman microscopy system (Witec Alpha 300, Germany) with a 532 nm excitation laser. The laser power was set to 0.8 mW. To obtain high signal-to-noise ratio spectral data, the integration time for a single spectrum was set to 1 s, accumulated over 10 scans. For high-resolution Raman and PL mapping, the integration time per pixel was set to 0.2 s, with 3 points scanned per μm. SHG response tests were conducted using a confocal Raman microscope system (Witec Alpha 300, Germany) with an incident laser wavelength of 1064 nm. The integration time was set to 0.5 s. The heat evacuation was characterized using SThM

(NT-MDT NTEGRA P9, Russia). All the electrical and photoelectric properties were measured using a probe-station equipped with a Keithly 2636B source meter unit. The 532 nm laser was used as the light source for photoelectric measurement, and its power was adjusted by rotating the light attenuator and verified by a power meter. Note that all the device fabrication and measurements were performed under ambient air condition.

Electronic Supplementary Material: Supplementary material (the orientation determination and stacking strategy of MoS_2/CrOCl heterostructures based on polarization-dependent optical anisotropy (Fig. S1), AFM characterization of the representative CrOCl thin flake (Fig. S2), optical microscopy and Raman spectroscopic characterization of annealed and exfoliated MoS_2/CrOCl heterostructures (Figs. S3 and S5), Raman mapping confirming interfacial uniformity (Fig. S4), photoluminescence spectra, AFM morphology, and scanning thermal microscopy images of the heterostructures (Figs. S6–S8), and Gaussian multi-peak deconvolution parameters of the PL spectra used to evaluate excitonic components and interlayer charge-transfer effects (Table S1)) is available in the online version of this article at https://doi.org/10.26599/NR.2026.94908743.

Data availability

All data needed to support the conclusions in the paper are presented in the manuscript and the Electronic Supplementary Material. Additional data related to this paper may be requested from the corresponding author upon request.

Acknowledgements

This work was supported by Innovation Research Foundation of National University of Defense Technology, Hunan Provincial Natural Science Foundation of China (No. 2026JJ50369).

Declaration of competing interest

All the contributing authors report no conflict of interests in this work.

Author contribution statement

C. Y. D. conceived the idea and designed experiments. G. P., W. L., G. W., H. M. Z., and S. F. L. supervised the overall project. W. Q. W., C. Y. Z., and J. Y fabricated the devices. J. Y. and J. H. X. performed electrical measurements and thermal characterization. T. Z. and J. Y. performed photodetection. J. Y. carried out Raman analysis and discussed on material characterization. C. Y. D., J. Y., and T. Z. conducted data analysis. C. Y. D., J. Y., and G. P. wrote and revised the manuscript. All the authors participated in the discussion of the results.

Use of AI statement

None.

References

[1] Zheng, X. M.; Wei, Y. H.; Zhang, X. Z.; Wei, Z. H.; Luo, W.; Guo, X.; Liu, J. X.; Peng, G.; Cai, W. W.; Huang, H. et al. Symmetry engineering induced in-plane polarization in MoS_2 through van der Waals interlayer coupling. *Adv. Funct. Mater.* **2022**, *32*, 2202658.

[2] Zhang, X.; Xie, X.; Li, S. F.; Chen, J. Y.; He, J.; Liu, Z. W.; Wang, J. T.; Liu, Y. P. Layer-dependent modulation of optical anisotropy in MoS_2/ReS_2 van der Waals heterostructures. *Nano Res.* **2025**, *18*, 94907365.

[3] Wang, P.; Zong, Y. X.; Liu, H.; Wen, H. Y.; Liu, Y. Y.; Wu, H. B.; Xia, J. B. Vertical strain and electric field tunable band alignment in type-II ZnO/MoSSe van der Waals heterostructures. *Phys. Chem. Chem. Phys.* **2021**, *23*, 1510–1519.

[4] Zhu, T.; Liu, K.; Zhang, Y.; Meng, S.; He, M. F.; Zhang, Y. L.; Yan, M. L.; Dong, X. X.; Li, X. B.; Jiang, M. et al. Gate voltage- and bias voltage-tunable staggered-gap to broken-gap transition based on WSe_2/Ta_2NiSe_5 heterostructure for multimode optoelectronic logic gate. *ACS Nano* **2024**, *18*, 11462–11473.

[5] Xia, J.; Yan, J. X.; Wang, Z. H.; He, Y. M.; Gong, Y. J.; Chen, W. Q.; Sum, T. C.; Liu, Z.; Ajayan, P. M.; Shen, Z. X. Strong coupling and pressure engineering in WSe_2–$MoSe_2$ heterobilayers. *Nat. Phys.* **2021**, *17*, 92–98.

[6] Ren, W. J.; Lu, S.; Yu, C. Q.; He, J.; Zhang, Z. W.; Chen, J.; Zhang, G. Impact of moiré superlattice on atomic stress and thermal transport in van der Waals heterostructures. *Appl. Phys. Rev.* **2023**, *10*, 041404.

[7] Xie, S. E.; Faeth, B. D.; Tang, Y. H.; Li, L. Z.; Gerber, E.; Parzyck, C. T.; Chowdhury, D.; Zhang, Y. H.; Jozwiak, C.; Bostwick, A. et al. Strong interlayer interactions in bilayer and trilayer moiré superlattices. *Sci. Adv.* **2022**, *8*, eabk1911.

[8] Quan, J. M.; Linhart, L.; Lin, M. L.; Lee, D.; Zhu, J. H.; Wang, C. Y.; Hsu, W. T.; Choi, J.; Embley, J.; Young, C. et al. Phonon renormalization in reconstructed MoS_2 moiré superlattices. *Nat. Mater.* **2021**, *20*, 1100–1105.

[9] Guo, Y. M.; Li, J. X.; Zhan, X. P.; Wang, C. W.; Li, M.; Zhang, B.; Wang, Z. R.; Liu, Y. Y.; Yang, K. N.; Wang, H. et al. van der Waals polarity-engineered 3D integration of 2D complementary logic. *Nature* **2024**, *630*, 346–352.

[10] Wu, S.; Wang, J. F.; Xie, H. Q.; Guo, Z. X. Interfacial thermal conductance across graphene/MoS_2 van der Waals heterostructures. *Energies* **2020**, *13*, 5851.

[11] Quan, Y. J.; Liao, B. L. Coupled electron–phonon hydrodynamics in two-dimensional semiconductors. *Phys. Rev. Lett.* **2025**, *134*, 226301.

[12] Fu, J. H.; Xu, Q.; Han, G. F.; Wu, B.; Huan, C. H. A.; Leek, M. L.; Sum, T. C. Hot carrier cooling mechanisms in halide perovskites. *Nat. Commun.* **2017**, *8*, 1300.

[13] Macheda, F.; Barone, P.; Mauri, F. Electron–phonon interaction and longitudinal-transverse phonon splitting in doped semiconductors. *Phys. Rev. Lett.* **2022**, *129*, 185902.

[14] Poncé, S.; Royo, M.; Stengel, M.; Marzari, N.; Gibertini, M. Long-range electrostatic contribution to electron–phonon couplings and mobilities of two-dimensional and bulk materials. *Phys. Rev. B* **2023**, *107*, 155424.

[15] Giustino, F. Electron–phonon interactions from first principles. *Rev. Mod. Phys.* **2017**, *89*, 015003.

[16] Quan, J. M.; Linhart, L.; Lin, M. L.; Lee, D.; Zhu, J. H.; Wang, C. Y.; Hsu, W. T.; Choi, J.; Embley, J.; Young, C. et al. Publisher correction: Phonon renormalization in reconstructed MoS_2 moiré superlattices. *Nat. Mater.* **2021**, *20*, 1167.

[17] Lin, M. L.; Zhou, Y.; Wu, J. B.; Cong, X.; Liu, X. L.; Zhang, J.; Li, H.; Yao, W.; Tan, P. H. Cross-dimensional electron–phonon coupling in van der Waals heterostructures. *Nat. Commun.* **2019**, *10*, 2419.

[18] Tang, Y.; Ping, Y.; Yang, X. X.; Xing, J. B.; Chen, J. B.; Wang, X.; Lu, J. B.; Jing, H. M.; Liu, K. Q.; Wu, J. X. et al. Synthesis of highly anisotropic 2D insulator CrOCl nanosheets for interfacial symmetry breaking in isotropic 2D semiconductors. *Adv. Mater.* **2025**, *37*, 2405358.

[19] Lee, C.; Yan, H. G.; Brus, L. E.; Heinz, T. F.; Hone, J.; Ryu, S.

Anomalous lattice vibrations of single- and few-layer MoS_2. *ACS Nano* **2010**, *4*, 2695–2700.

[20] Li, H.; Zhang, Q.; Yap, C. C. R.; Tay, B. K.; Edwin, T. H. T.; Olivier, A.; Baillargeat, D. From bulk to monolayer MoS_2: Evolution of Raman scattering. *Adv. Funct. Mater.* **2012**, *22*, 1385–1390.

[21] Zheng, X. M.; Wei, Y. H.; Wei, Z. H.; Luo, W.; Guo, X.; Zhang, X. Z.; Liu, J. X.; Chen, Y. B.; Peng, G.; Cai, W. W. et al. Highly anisotropic thermal conductivity of few-layer CrOCl for efficient heat dissipation in graphene device. *Nano Res.* **2022**, *15*, 9377–9385.

[22] Jiang, X.; Kang, L.; Huang, B. Role of interlayer coupling in second harmonic generation in bilayer transition metal dichalcogenides. *Phys. Rev. B* **2022**, *105*, 045415.

[23] Shree, S.; Lagarde, D.; Lombez, L.; Robert, C.; Balocchi, A.; Watanabe, K.; Taniguchi, T.; Marie, X.; Gerber, I. C.; Glazov, M. M. et al. Interlayer exciton mediated second harmonic generation in bilayer MoS_2. *Nat. Commun.* **2021**, *12*, 6894.

[24] Yuan, Y. J.; Liu, P.; Wu, H. J.; Chen, H. T.; Zheng, W. H.; Peng, G.; Zhu, Z. H.; Zhu, M. J.; Dai, J. Y.; Qin, S. Q. et al. Probing the twist-controlled interlayer coupling in artificially stacked transition metal dichalcogenide bilayers by second-harmonic generation. *ACS Nano* **2023**, *17*, 17897–17907.

[25] Wu, L. S.; Cong, C. X.; Shang, J. Z.; Yang, W. H.; Chen, Y.; Zhou, J. D.; Ai, W.; Wang, Y. L.; Feng, S.; Zhang, H. B. et al. Raman scattering investigation of twisted WS_2/MoS_2 heterostructures: Interlayer mechanical coupling versus charge transfer. *Nano Res.* **2021**, *14*, 2215–2223.

[26] Pandey, V.; Mishra, S.; Maity, N.; Paul, S.; B, A. M.; Roy, A. K.; Glavin, N. R.; Watanabe, K.; Taniguchi, T.; Singh, A. K. et al. Probing interlayer interactions and commensurate–incommensurate transition in twisted bilayer graphene through Raman spectroscopy. *ACS Nano* **2024**, *18*, 4756–4764.

[27] Wei, Z. H.; Zheng, X. M.; Wei, Y. H.; Zhang, X. Z.; Luo, W.; Liu, J. X.; Peng, G.; Huang, H.; Lv, T. Y.; Zhang, X. A. et al. van der Waals interlayer coupling induces distinct linear dichroism in WSe_2 photodetectors. *Adv. Opt. Mater.* **2023**, *11*, 2201962.

[28] Zheng, M. M.; Liu, J. X.; Luo, C. B.; Ge, Y. N.; Cao, Y.; Huang, C. Y.; Yang, J.; Luo, S. F.; Cheng, T. Q.; Lin, M. Y. et al. Synergistic bridgeable charge transfer for photoluminescence modulation in wedding-cake-like MoS_2/CrOCl heterostructures. *Adv. Opt. Mater.* **2025**, *13*, 2403492.

[29] Rao, R.; Islam, A. E.; Singh, S.; Berry, R.; Kawakami, R. K.; Maruyama, B.; Katoch, J. Spectroscopic evaluation of charge-transfer doping and strain in graphene/MoS_2 heterostructures. *Phys. Rev. B* **2019**, *99*, 195401.

[30] Ji, E. J.; Yang, K. M.; Shin, J. C.; Kim, Y.; Park, J. W.; Kim, J.; Lee, G. H. Exciton-dominant photoluminescence of MoS_2 by a functionalized substrate. *Nanoscale* **2022**, *14*, 14106–14112.

[31] Hong, X. P.; Kim, J.; Shi, S. F.; Zhang, Y.; Jin, C. H.; Sun, Y. H.; Tongay, S.; Wu, J. Q.; Zhang, Y. F.; Wang, F. Ultrafast charge transfer in atomically thin MoS_2/WS_2 heterostructures. *Nat. Nanotechnol.* **2014**, *9*, 682–686.

[32] Yuan, J. T.; Najmaei, S.; Zhang, Z. H.; Zhang, J.; Lei, S. D.; Ajayan, P. M.; Yakobson, B. I.; Lou, J. Photoluminescence quenching and charge transfer in artificial heterostacks of monolayer transition metal dichalcogenides and few-layer black phosphorus. *ACS Nano* **2015**, *9*, 555–563.

[33] Mak, K. F.; He, K. L.; Lee, C.; Lee, G. H.; Hone, J.; Heinz, T. F.; Shan, J. Tightly bound trions in monolayer MoS_2. *Nat. Mater.* **2013**, *12*, 207–211.

[34] Ramos, M.; Marques-Moros, F.; Esteras, D. L.; Mañas-Valero, S.; Henríquez-Guerra, E.; Gadea, M.; Baldoví, J. J.; Canet-Ferrer, J.; Coronado, E.; Calvo, M. R. Photoluminescence enhancement by band alignment engineering in $MoS_2/FePS_3$ van der Waals heterostructures. *ACS Appl. Mater. Interfaces* **2022**, *14*, 33482–33490.

[35] Kistner-Morris, J.; Shi, A.; Liu, E. F.; Arp, T.; Farahmand, F.; Taniguchi, T.; Watanabe, K.; Aji, V.; Lui, C. H.; Gabor, N. Electric-field tunable Type-I to Type-II band alignment transition in $MoSe_2/WS_2$ heterobilayers. *Nat. Commun.* **2024**, *15*, 4075.

[36] Mak, K. F.; Lee, C.; Hone, J.; Shan, J.; Heinz, T. F. Atomically thin MoS_2: A new direct-gap semiconductor. *Phys. Rev. Lett.* **2010**, *105*, 136805.

[37] Luo, H. L.; Li, X. Y.; Zhao, Y. C.; Yang, R.; Bao, L. H.; Hao, Y. F.; Gao, Y. N.; Shi, N. N.; Guo, Y.; Liu, G. D. et al. Simultaneous generation of direct- and indirect-gap photoluminescence in multilayer MoS_2 bubbles. *Phys. Rev. Mater.* **2020**, *4*, 074006.

[38] Liu, Y. J.; Sun, M.; Pei, W. Y.; Zhang, T. Y.; Guo, Y. M.; Wang, H. W. Anisotropic conductance in a charge-transferred p-type 2D semiconductor. *J. Mater. Sci. Technol.* **2026**, *263*, 169–174.

[39] Pan, Y. M.; Hildebrandt, P. N.; Zahn, D.; Zacharias, M.; Windsor, Y. W.; Ernstorfer, R.; Caruso, F.; Seiler, H. Momentum-resolved signatures of carrier screening effects on electron–phonon coupling in MoS_2. *ACS Nano* **2025**, *19*, 11381–11389.

[40] Jin, C. H.; Kim, J.; Suh, J.; Shi, Z. W.; Chen, B.; Fan, X.; Kam, M.; Watanabe, K.; Taniguchi, T.; Tongay, S. et al. Interlayer electron–phonon coupling in WSe_2/hBN heterostructures. *Nat. Phys.* **2017**, *13*, 127–131.

[41] Bampoulis, P.; van Bremen, R.; Yao, Q. R.; Poelsema, B.; Zandvliet, H. J. W.; Sotthewes, K. Defect dominated charge transport and Fermi level pinning in MoS_2/metal contacts. *ACS Appl. Mater. Interfaces* **2017**, *9*, 19278–19286.

[42] Li, Y. F.; Wu, J.; Luo, J.; Wang, J. L.; Yu, W.; Cao, B. Y. Quantitative measurements in scanning thermal microscopy: Theoretical models, calibration technique, and integrated instrument. *J. Appl. Phys.* **2025**, *138*, 050701.

[43] Swoboda, T.; Wainstein, N.; Deshmukh, S.; Köroğlu, Ç.; Gao, X.; Lanza, M.; Hilgenkamp, H.; Pop, E.; Yalon, E.; Muñoz Rojo, M. Nanoscale temperature sensing of electronic devices with calibrated scanning thermal microscopy. *Nanoscale* **2023**, *15*, 7139–7146.

[44] Li, X.; Wu, D.; Lin, P.; Han, B.; Shi, Z. F.; Tian, Y. T.; Li, X. J.; Zeng, L. H. Low-temperature synthesis of wafer-scale 2D topological semimetal $NiTe_2$ for high-efficiency broadband photodetection and imaging. *Laser Photonics Rev.* **2025**, *19*, e01119.

[45] Li, X.; Liu, K. X.; Wu, D.; Lin, P.; Shi, Z. F.; Li, X. J.; Zeng, L. H.; Chai, Y.; Lau, S. P.; Tsang, Y. H. Van der Waals hybrid integration of 2D semimetals for broadband photodetection. *Adv. Mater.* **2025**, *37*, 2415717.